



**HAL**  
open science

# CFD-guided patterning of tubular ceramic membrane surface by stereolithography: Optimizing morphology at the mesoscale for improved hydrodynamic control of membrane fouling

Cyril Chevarin, Xunhao Wang, Denis Bouyer, Volodymyr Tarabara, Thierry Chartier, André Ayrat

## ► To cite this version:

Cyril Chevarin, Xunhao Wang, Denis Bouyer, Volodymyr Tarabara, Thierry Chartier, et al.. CFD-guided patterning of tubular ceramic membrane surface by stereolithography: Optimizing morphology at the mesoscale for improved hydrodynamic control of membrane fouling. *Journal of Membrane Science*, 2023, *Journal of Membrane Science*, pp.121435. 10.1016/j.memsci.2023.121435 . hal-03967704

**HAL Id: hal-03967704**

**<https://unilim.hal.science/hal-03967704>**

Submitted on 3 Oct 2023

**HAL** is a multi-disciplinary open access archive for the deposit and dissemination of scientific research documents, whether they are published or not. The documents may come from teaching and research institutions in France or abroad, or from public or private research centers.

L'archive ouverte pluridisciplinaire **HAL**, est destinée au dépôt et à la diffusion de documents scientifiques de niveau recherche, publiés ou non, émanant des établissements d'enseignement et de recherche français ou étrangers, des laboratoires publics ou privés.

# CFD-guided patterning of tubular ceramic membrane surface by stereolithography: Optimizing morphology at the mesoscale for improved hydrodynamic control of membrane fouling

Cyril Chevarin<sup>1</sup>, Xunhao Wang<sup>2</sup>, Denis Bouyer<sup>1\*</sup>, Volodymyr V. Tarabara<sup>2\*\*</sup>, Thierry Chartier<sup>3</sup>, André Ayrat<sup>1</sup>

<sup>1</sup> *Institut Européen des Membranes IEM – UMR 5635, ENSCM, CNRS, Univ Montpellier, Montpellier, France*

<sup>2</sup> *Department of Civil and Environmental Engineering, Michigan State University, East Lansing, MI 48824, USA*

<sup>3</sup> *CNRS, University of Limoges, Institute of Research for Ceramics (IRCER), UMR 7315, European Ceramics Center, Limoges, France*

## Abstract

A preliminary study was carried out on the morphological design of tubular single-channel alumina membranes prepared by stereolithography, an additive manufacturing process. The geometry of the ring-patterned inner surface of membranes was optimized using computational fluid dynamics calculations and validated in microfiltration tests with aqueous suspensions of *P. aeruginosa*. Patterning of the inner surface of tubular membranes helped reduce cake formation at a higher value of the average crossflow velocity. The results highlight benefits of stereolithography-based approach to the morphological design of ceramic membranes.

**Keywords:** ceramic membrane, computational fluid dynamics, stereolithography, fouling

\* Corresponding author. *Institut Européen des Membranes, Univ Montpellier, Montpellier, France*

\*\* Corresponding author. *Department of Civil and Environmental Engineering, Michigan State University, East Lansing, USA*

E-mail addresses: denis.bouyer@umontpellier.fr (D. Bouyer), tarabara@msu.edu (V. V. Tarabara).

## 1. Introduction

Rapid advances in additive manufacturing have paved the way for the simplified fabrication of integrated systems as well as system components with complex shapes hitherto inaccessible by conventional manufacturing methods. It is particularly the case for ceramic materials [1-3], which require high temperature sintering to confer morphological, microstructural and mechanical properties to the shaped object. These advances open up new possibilities for the design of ceramic membranes with materials. Indeed, there is a growing interest in the use of additive manufacturing methods to prepare both membranes, including ceramic filters [4-6], and membrane modules [7-11].

Many of the current membrane processes are based on the principle of crossflow filtration, with key concerns regarding the minimization of concentration polarization and fouling. Fouling management often requires a regular interruption of the filtration process by cleaning sequences (e. g. backwashing) limits the lifetime of the membranes. A complementary approach to minimizing fouling and its deleterious

effects effects is to promote turbulence in the feed flow. The use of turbulence promoters is possible but at a cost of an increased pressure drop in the feed flow channel. Another option is to promote turbulence closer to the membrane surface by altering its topography. This has been the subject of various studies, most of which focused on the surface patterning of polymer membranes [12-14] although some did employ flat plate ceramic membranes [15, 16].

Most installations use ceramic membranes in a tubular configuration, the support of which is produced by extrusion. Based on a computational fluid dynamics (CFD) approach, Yang et al. explored optimization of multi-channel ceramic membranes [17]. While the number and the section of the channels are easily adjustable, the same cannot be said for their surface morphology. Twenty years ago a clever method was developed, allowing the extrusion of tubular supports with a spiral internal surface favoring the turbulence of the flow [18]. During the 2018 International Conference in Inorganic Membranes, a presentation by TAMI Industries highlighted the CFD-based prediction of the benefits of having curvilinear flow inside a tubular membrane channel, the practical implementation of such flow field using bundles of helical membranes, as well as the potential of additive processes for manufacturing such membranes [19].

The present work concerns a preliminary study on the morphological design of ceramic tubular membranes. Single-channel alumina tubular membranes with an inner diameter of 7 mm and an outer diameter of 10 mm were selected, corresponding to usual specifications for current commercial membranes of this type. The inner surface the membrane was patterned with rings – nmorphological elements that cannot be introduced at the membrane surface by the conventional shaping method based on paste extrusion. The ring profile and height as well as the inter-ring distance were optimized using CFD modeling by evaluating the impact of these parameters on the turbulence near the membrane surface. CFD predictions were validated in preliminary experiments with symmetric alumina microfiltration (pore diameter of  $\sim 0.2 \mu\text{m}$ ) membranes, with or without such rings, manufactured by an additive process (i. e. stereolithography) from alpha alumina powder. The patterned membranes and smooth membranes (controls) were comparatively evaluated in terms of fouling behavior in experiments with *P. aeruginosa* suspensions.

## **2. Numerical model**

### **2.1. Geometry**

The flow hydrodynamics in the tubular membranes was simulated for both smooth and patterned membranes as shown in Figure 1. Here, “patterned” refers to a membrane with the inner (feed-facing) surface having a patterned morphology. In both configurations (smooth or patterned inner surface), the outer diameter and the membrane length were 10 mm and 50 mm, respectively. The inner diameter of both membranes was 7 mm everywhere except in locations corresponding to roughness elements (“rings”) on the surface of the patterned membrane; each such “ring” was  $\sim 0.5$  mm high, leading to a somewhat smaller inner diameter in those locations. Thanks to the axial symmetry, simulations were performed using 2D axisymmetric geometry thus notably reducing the calculation time.

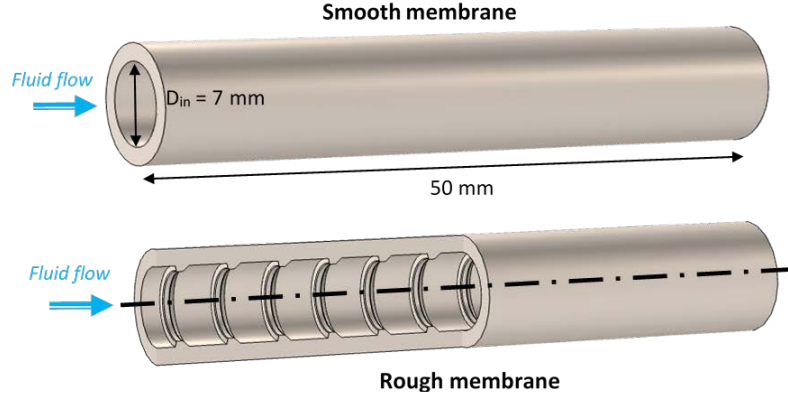


Figure 1. Geometry of smooth and patterned tubular membranes.

## 2.2. Governing equations

Two feed flow rates were simulated herein, with mean velocities of  $0.45 \text{ m}\cdot\text{s}^{-1}$  and  $0.68 \text{ m}\cdot\text{s}^{-1}$ , respectively in agreement with the values used in filtration experiments. Given the density and viscosity of water at  $23 \text{ }^\circ\text{C}$ , the diameter of the flow channel, and the two mean velocities, Reynolds numbers of 3100 and 4830, respectively were calculated, corresponding to the end of the transition zone between laminar and turbulent hydrodynamic regimes. Consequently, the classical Reynolds Averaged Navier–Stokes (RANS) transport equations for incompressible Newtonian fluid and turbulent regime were used in the model.

In the RANS model, the conservation of momentum equation is given by:

$$\rho(\nabla \cdot \vec{v})\vec{v} = -\nabla p + \nabla \cdot ((\eta + \eta_t)[(\nabla \vec{v} + \nabla \vec{v}^T)]) + \rho \vec{g} \quad (1)$$

where  $\rho$  is the water bulk density ( $\text{kg}\cdot\text{m}^{-3}$ ),  $\vec{v}$  is the velocity vector ( $\text{m}\cdot\text{s}^{-1}$ ),  $p$  is the static pressure (Pa),  $[(\nabla \vec{v} + \nabla \vec{v}^T)] = \dot{\tau}$  is the viscous stress tensor,  $\eta$  is the dynamic viscosity of the water (Pa.s),  $\eta_t$  is the turbulent (or eddy) viscosity (Pa.s) and  $\vec{g}$  is the acceleration due to gravity ( $\text{m}\cdot\text{s}^{-2}$ ).

The standard k- $\epsilon$  model [20] (see Supplementary Information (SI), section S1) was used to simulate the turbulence, meaning that the turbulent viscosity  $\eta_t$  was modeled using eq. (2) [21]:

$$\eta_t = \rho C_\eta \frac{k^2}{\epsilon}, \quad (2)$$

where  $C_\eta$  is a constant,  $k$  is the turbulent kinetic energy ( $\text{m}^2\cdot\text{s}^{-2}$ ) and  $\epsilon$  is the turbulent energy dissipation rate ( $\text{m}^2\cdot\text{s}^{-3}$ ).

## 2.3. Boundary conditions

Fully developed flow with a mean velocity (in  $\text{m}\cdot\text{s}^{-1}$ ) was considered in the model for boundary conditions in the inlet side. Two mean velocities were simulated, i. e.  $0.45 \text{ m}\cdot\text{s}^{-1}$  and  $0.68 \text{ m}\cdot\text{s}^{-1}$ . At the outlet side, a null static pressure boundary condition  $P_0$  was fixed. A no-slip boundary condition was applied at the wall.

## 2.4. Numerical simulations

The hydrodynamic model was simulated using the commercial COMSOL Multiphysics® software, working with finite element method. Using a 2D axis-symmetric model, meshes size was ranged between 0.08 mm near the wall and 0.2 mm in the bulk of the flow. Boundaries layers and finer meshes were built near the wall surfaces to improve the numerical accuracy in the boundary layer. The number of tetrahedral meshes was close to 100 000 for the simulations without rings and 140 000 for the simulations with rings.

### **3. Experimental**

#### ***3.1. Membrane manufacturing and microstructural characterization***

The membranes were manufactured by the company 3DCERAM SINTO (Limoges, France) according to our specifications. The green bodies were built using the stereolithography additive process (CERAMAKER 900 machine) based on the selective polymerization of a reactive mixture system under the effect of a UV irradiation. The reactive system was a suspension of alumina particles (1.75  $\mu\text{m}$  mean particle size) in a mixture of curable monomer and oligomer, with the addition of a photoinitiator. After debinding and sintering, the pieces were externally machined to achieve the requested dimensional specifications (outer diameter =  $10.0 \pm 0.2$  mm; inner diameter =  $7.0 \pm 0.2$  mm; length =  $49.2 \pm 0.2$  mm).

For the rough membranes, the targeted characteristics for rings were as follows: height of 500  $\mu\text{m}$ ; a symmetrical profile with the first and second edges (considering the flow direction) forming an angle of  $10^\circ$  and  $45^\circ$ , respectively, the vertical of the surface of the rings; distance between two successive rings of 3 mm. The geometry of these rough membranes was confirmed by making a cutout in one of these tubes using a diamond saw, observing this sample by Keyence VHX 6000 digital microscope (VHX) and then analyzing the Keyence images with suitable software (VHX-6000\_950F).

The microstructure of the membranes was investigated using a Field Emission Scanning Electron Microscope (FE-SEM; Hitachi S4800). The porosity of these macroporous samples was determined by mercury porosimetry (AutoPore IV 9500 Micromeritics).

#### ***3.2. Fouling experiments***

##### ***3.2.1. Experimental setup and membrane permeability measurements***

The membranes were tested using a crossflow filtration system (see SI, Figure S1), which included a peristaltic pump (910-0025, Thermo Scientific), a custom-made membrane unit and a back-pressure valve (SS-43S6, Swagelok). The membrane was mounted using two stainless steel push-to-connect fittings (KQG2H10-00, Grainger). To seal the membrane area under the fittings and ensure it is not available for permeation, the outside surface of the membrane under the fittings was coated with a thin layer of epoxy (LOCTITE, Henkel). The pure water flux tests for the 3D-printed membranes were performed using DI water and five different transmembrane pressure values: 1.03, 1.38, 1.72, 2.07, and 2.41 bar (15, 20, 25, 30, and 35 psi, respectively). The DI water (pH 5.8) was used as the feed solution in these tests. The crossflow velocity was maintained constant at either  $0.45 \text{ m}\cdot\text{s}^{-1}$  or  $0.68 \text{ m}\cdot\text{s}^{-1}$ . The permeability of each membrane was calculated based on the slope of the flux vs pressure dependence.

##### ***3.2.2. Bacterial suspensions: Preparation and characterization***

An aqueous suspension of *P. aeruginosa* (Schroeter) Migula (PA01-LAC, ATCC) was used as the feed in membrane fouling tests. PA01 was cultured in Luria-Bertani (LB) broth to the exponential growth phase. The standard curve (colony-forming units per milliliter (CFU/ml) vs absorbance at 600 nm) was established. The preparation of the bacteria stock is detailed in the SI file, section S2. The bacteria were enumerated by a colony count method. Briefly, the vortexed solutions were serially diluted, mixed with soft agar, and poured onto LB-agar plates, which were incubated at 37 °C overnight. The formed colonies were counted, and then the areal density of colony-forming units (CFU/ml) was calculated. The absorbance of the bacterial suspensions was measured by a spectrophotometer (Spectronic 21D). The hydrodynamic diameter of bacteria was measured by dynamic light scattering (DLS). In these tests, a small sample (0.5 mL) of the bacterial suspension was diluted in 1 mM KCL solution, prefiltered with 0.22 µm syringe filter, to the total volume of ~ 2 mL.

### 3.2.3. Membrane fouling tests

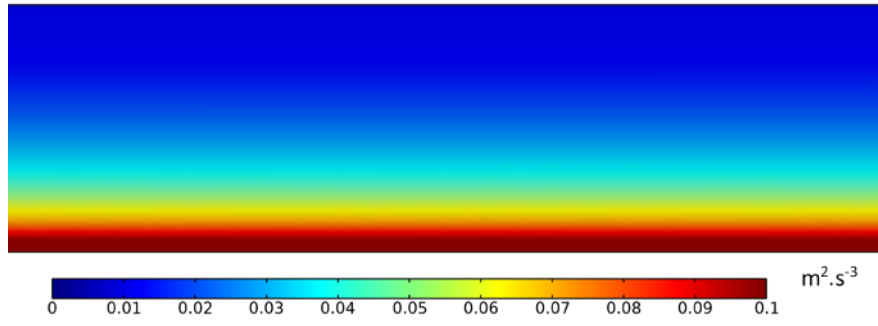
Prior to each crossflow filtration test, the feed suspension was prepared by diluting the bacteria stock ten-fold with DI water. The volume fraction of PA01 in the feed was  $3.9 \cdot 10^{-5}$ . Based on this very low value and the Einstein relation between relative viscosity and volume fraction of dispersed phase [22], the viscosity of this suspension was considered to be equal to that of pure water. The ionic strength of the feed was 15 mM. During fouling tests, the crossflow velocity (averaged across the membrane channel cross-section) was  $0.45 \text{ m}\cdot\text{s}^{-1}$  or  $0.68 \text{ m}\cdot\text{s}^{-1}$ , which corresponded to the maximum crossflow rate ( $1570 \text{ mL}\cdot\text{min}^{-1}$ ) that the peristaltic pump could provide. Prior to challenging the membrane with the bacterial suspension, the membrane was equilibrated with 15 mM NaCl at pH 6. The permeate was collected on a mass balance with a 1 min interval. All fouling tests were done at the ambient temperature of 23 °C and the relative humidity of 47%. After each fouling test, the membrane was cleaned by circulating solutions in the feed channel in the following sequence: (1) DI water for 30 min, (2) 5 mM EDTA at pH 11 for 30min, (3) DI water for 30 min, (4) 2 mM SDS at pH 11 for 30 min, (5) DI water for 30 min [23].

Three smooth and three rough membranes were tested under the same experimental conditions to estimate the reproducibility of the results. In order to investigate the contribution of the different fouling mechanisms to the overall decline in permeate flux, additional tests were carried out in the dead-end filtration regime following a procedure described earlier [24].

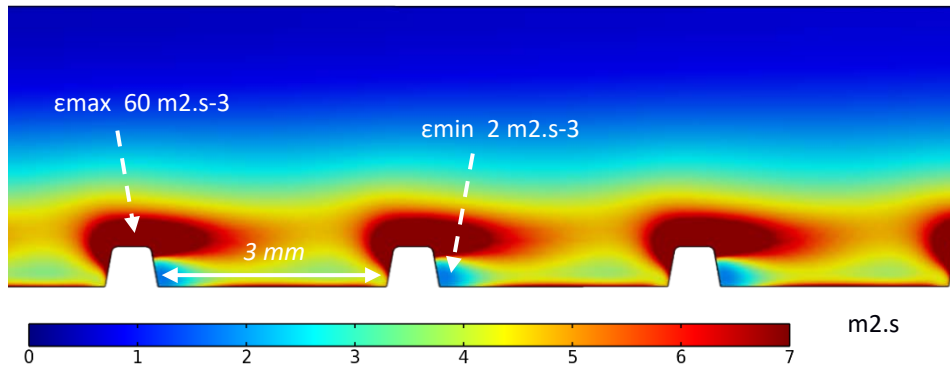
## 4. Results and discussion

### 4.1. Membrane design from numerical simulations

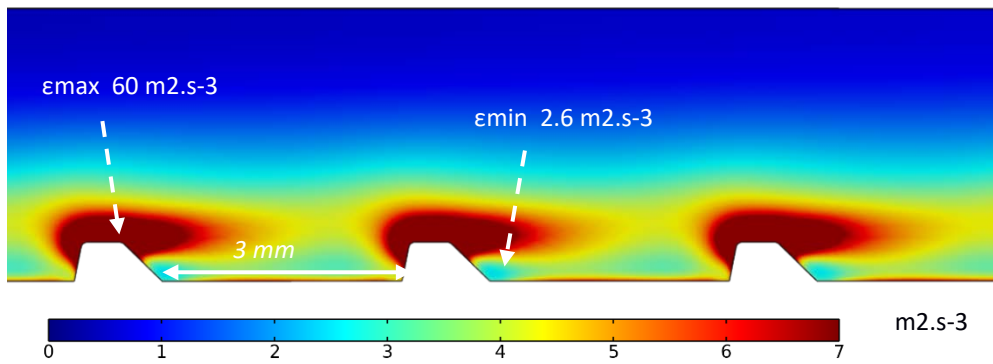
As already said in the introduction, in the frame of this pioneering study, it was decided to pattern the inner surface of the tubular membranes with simple and continuous rings. The current limitations of the existing additive manufacturing in terms of dimensional tolerances were considered for sizing these rings. With the implemented technique, i.e. stereolithography, the dimensional resolution is about 100 µm [2]. It is the reason why rings with a height and a width of 500 µm were chosen.



(a) Smooth membrane

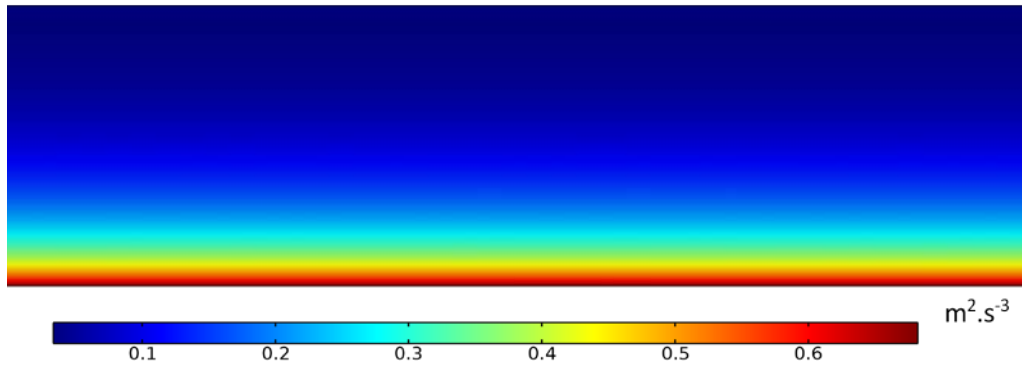


(b) Rough membrane – symmetrical profile

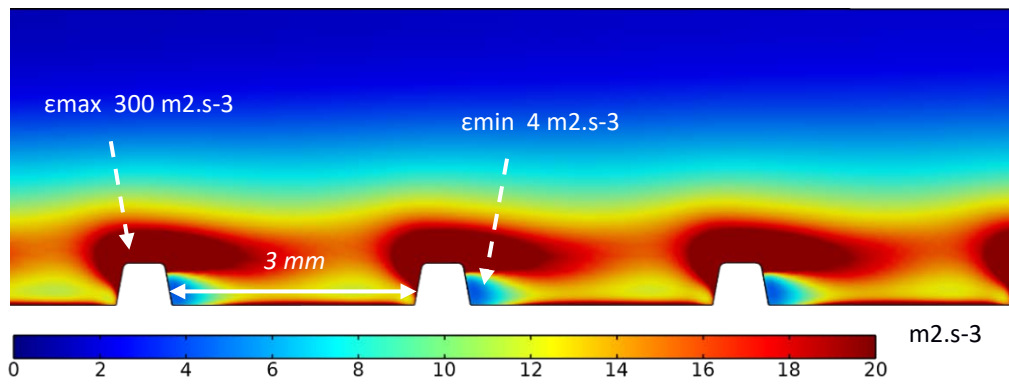


(c) Rough membrane – asymmetrical profile

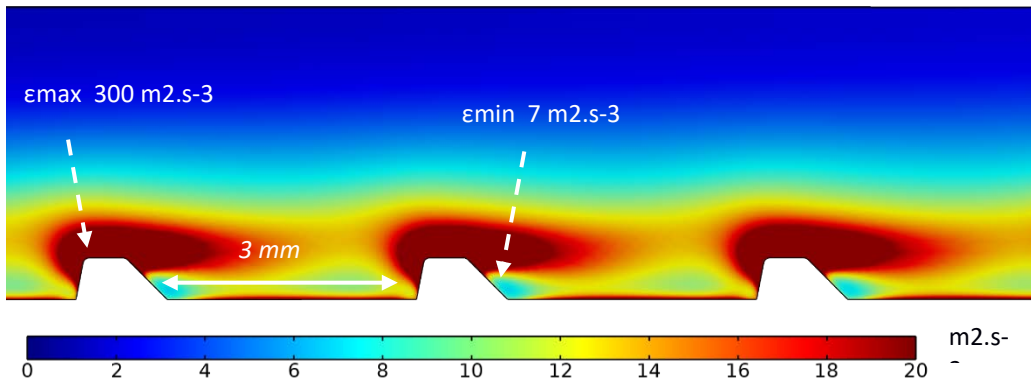
Figure 2. Dissipation rate of turbulent kinetic energy,  $\varepsilon$ , in the vicinity of the rings on the surface of the tubular membrane for  $v_{in} = 0.45 \text{ m}\cdot\text{s}^{-1}$ : (a) smooth membrane, (b) symmetrical profile, (c) asymmetrical profile.



(a) Smooth membrane



(b) Rough membrane – symmetrical profile of surface “rings”



(c) Rough membrane – asymmetrical profile of surface “rings”

Figure 3. Dissipation rate of turbulent kinetic energy,  $\epsilon$ , in the vicinity the rings on the surface of the tubular membrane for  $v_{in} = 0.68 \text{ m}\cdot\text{s}^{-1}$ : (a) smooth membrane, (b) rough membrane featuring “rings” with symmetrical profile, (c) rough membrane featuring surface “rings” with asymmetrical profile.

Figures 2 and 3 show the spatial distribution of the dissipation rate of turbulent kinetic energy,  $\epsilon$ , in three different configurations (smooth membrane, rough membrane and rings with symmetrical profile, rough membrane and rings with asymmetrical profile), for inlet velocities of  $0.45$  and  $0.68 \text{ m}\cdot\text{s}^{-1}$ , respectively.

Whatever the configuration,  $\varepsilon$  is much higher close to the top of the rings compared to the region between the rings, with a ratio close to 23 at  $0.45 \text{ m}\cdot\text{s}^{-1}$  and more than 42 at  $0.68 \text{ m}\cdot\text{s}^{-1}$ . A 50% increase in the inlet velocity (from  $0.45$  to  $0.68 \text{ m}\cdot\text{s}^{-1}$ ), leads to a five-fold increase in  $\varepsilon$  at the top of trgeh rings and a three-fold increase in  $\varepsilon$  between the rings. These results confirm the intuitive predictions, highlighting the interest to disturb the flow near the membrane surface to create more turbulence (more dissipation of turbulent kinetic energy). With this geometrical configuration, the risk lies in the formation of dead zone between the rings that is the zone with local re-circulation and characterized by a lower level of turbulence. Further, when analyzing the influence the ring shape (symmetric vs asymmetric), the numerical simulations clearly show that the low  $\varepsilon$  region, localized just downstream of each ring, is smaller behind rings with the asymmetrical profile. For both inlet velocities evaluated ( $0.45$  or  $0.68 \text{ m}\cdot\text{s}^{-1}$ ), asymmetry appears to be favorable for preventing fouling phenomena.

Based on these numerical results, the asymmetric profile was selected. The following study of the impact of the inter-ring distance (see SI, Figure S2) showed that it had a relatively minor effect on the spatial distribution of  $\varepsilon$ ; the inter-ring distance of 3 mm was selected as allowing the most reduction in the spatial extent of low  $\varepsilon$  zones.

Table 1 summarizes the values of the energy dissipation rate  $\varepsilon$  and the pressure loss along the membrane. These values give an indication of the cost of integrating the rings as turbulence promoters within the tubular membrane. Whatever the inlet velocity, the pressure loss increases by a factor 15 when using rough membranes rather than smooth ones. This result is not surprising because it is directly linked to the total dissipation rate of turbulent kinetic energy, and it should be related to the energy cost of back-washing frequency that should be done between two filtration cycles.

*Table 1. Specific pressure loss,  $\Delta P_{feed}$ , in the feed flow along the membrane and mean value of turbulent dissipation rate,  $\varepsilon_{mean}$ , at the membrane surface for two values of the average crossflow velocity,  $v_{in}$ . Turbulent dissipation rate is for the membrane surface between the rings and is deduced from the simulations graphically represented in Figure S2.*

	Smooth membrane		Rough membrane	
	$v_{in} = 0.45 \text{ m}\cdot\text{s}^{-1}$	$v_{in} = 0.68 \text{ m}\cdot\text{s}^{-1}$	$v_{in} = 0.45 \text{ m}\cdot\text{s}^{-1}$	$v_{in} = 0.68 \text{ m}\cdot\text{s}^{-1}$
$\varepsilon_{mean} \text{ (m}^2\cdot\text{s}^{-3}\text{)}$	0.10	0.45	4.6	16.3
$\Delta P_{feed} \text{ (bar}\cdot\text{m}^{-1}\text{)}$	0.006	0.013	0.092	0.204

Table 1 shows that a significant advantage can be expected with the rough membranes in terms of fouling limitation, especially for the largest value of average inlet crossflow velocity. The reported values of specific pressure loss in the feed flow qualitatively account for the additional energy cost associated with the use of rough membranes. The determined values are more than one order of magnitude larger for the rough membranes but rather low in absolute value.

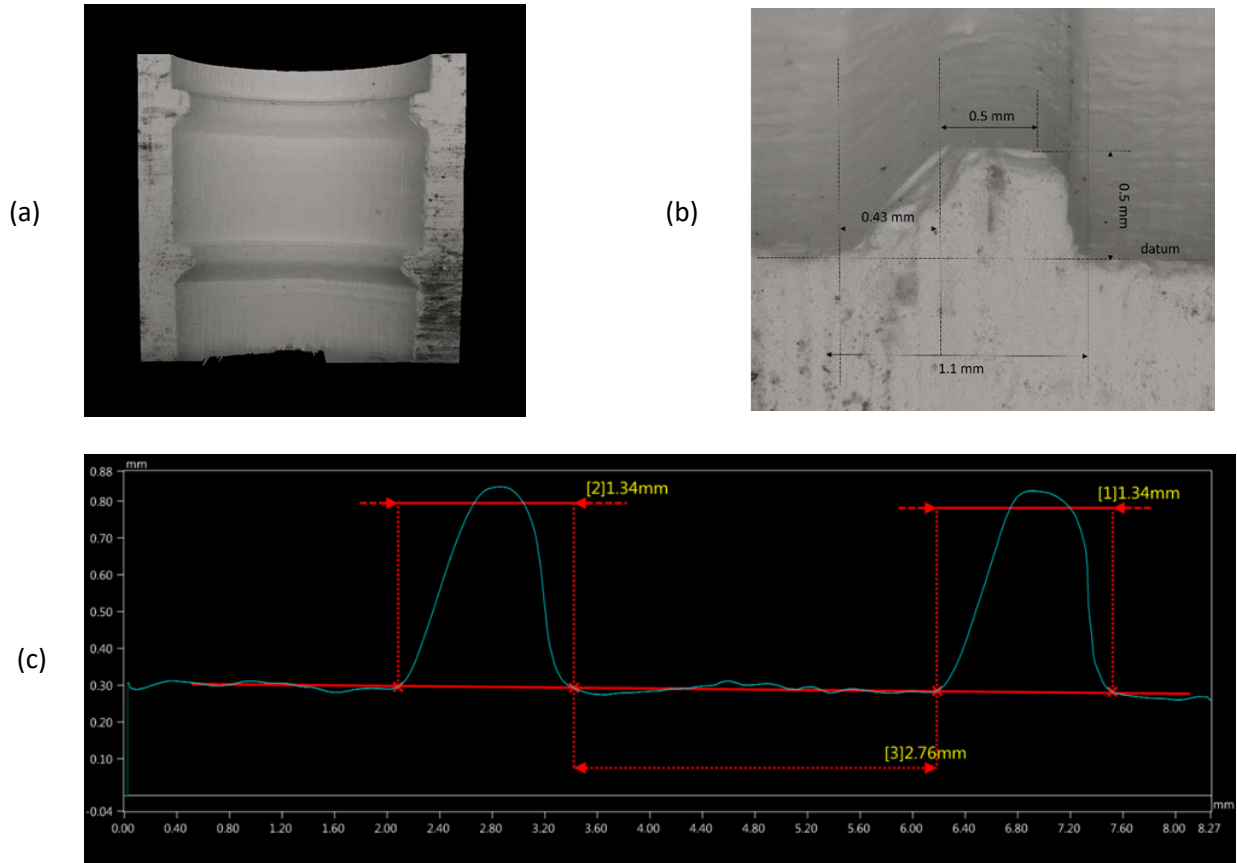


Figure 4. Geometry of the rough membrane: (a) image of the inner surface of the membrane cutout. (b) and (c): Characteristic sizes of roughness elements.

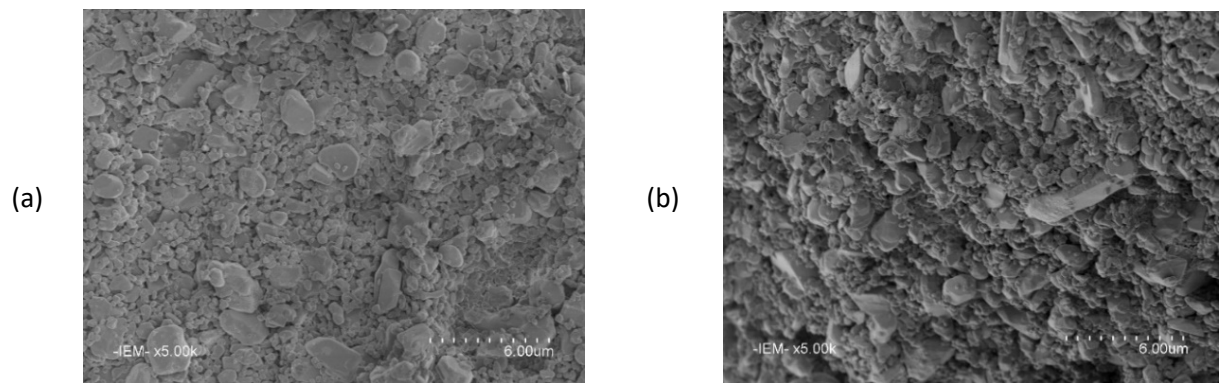


Figure 5. SEM images of the membrane: (a planar) surface and (b) cross section.

## 4.2. Microstructural characterization of the manufactured membranes

Figure 4 shows the internal morphology of the rough membranes with the axisymmetric structure of the roughness elements (“rings”) clearly shown (Figure 4a). The ring profile (Figure 4b) and the inter-ring spacing (Figure 4c) correspond rather well to the targeted characteristics considering the 100  $\mu\text{m}$  spatial resolution of the implemented additive method. SEM imaging of the planar surface (Figure 5a) and the cross-section (Figure 5b) of the membranes showed a close packing arrangement of grains with a bimodal size distribution. The continuous matrix with submicron porosity is embedded with grains several microns in size.

Mercury porosimetry measurements yielded the porosity of  $\sim 33\%$  and the specific surface area of  $\sim 2.5\text{ m}^2\text{ g}^{-1}$ . These values are consistent with what can be expected to result from the limited sintering of a random close-packing arrangement of powder particles. The pore size distribution (Figure 6) is centered around an average pore size of  $\sim 0.2\ \mu\text{m}$ . The prepared membranes can thus be classified as microfilters.

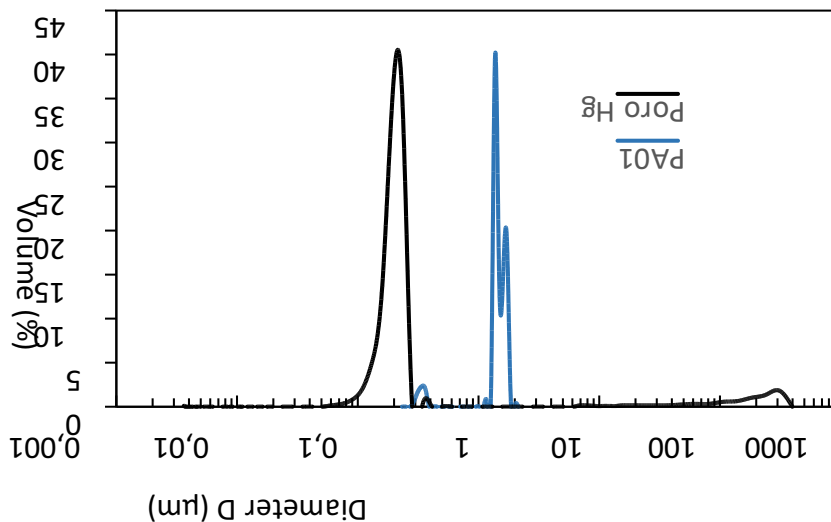


Figure 6. Pore size distribution of ceramic membranes and the size distribution of bacteria in the feed suspension.

## 4.3. Fouling experiments

Based on the DLS measurements, the average size of bacteria in the feed suspension was  $\sim 0.8\ \mu\text{m}$ , which is significantly larger than the measured average pore size ( $\sim 0.2\ \mu\text{m}$ ) of the membrane (Figure 6). The DLS measurements estimated the diffusion coefficient, which was then converted to particle size assuming that the scatterers are spherical.

Application of the Carman-Kozeny relation to mercury porosimetry data [25] estimates the intrinsic permeability of the membrane to be  $\sim 1.6 \cdot 10^{-16}\text{ m}^2$ . The expected water permeability at 23  $^{\circ}\text{C}$  is thus equal

to  $42 \pm 16 \text{ L}\cdot\text{m}^{-2}\cdot\text{h}^{-1}\cdot\text{bar}^{-1}$ , which is within the experimental error from the valued measured experimentally for a smooth membrane ( $69 \pm 15 \text{ L}\cdot\text{m}^{-2}\cdot\text{h}^{-1}\cdot\text{bar}^{-1}$ ).

The results obtained in crossflow filtration tests are summarized in Figure 7. Based on the application of Hermia blocking law analysis to dead end filtration data (see SI, Figures S3 and S4), two fouling regimes could be discerned: pore blockage and cake filtration. The presence of integrated rings had no effect on pore blockage but led to a significant mitigation of fouling in the cake filtration regime at the higher value of crossflow velocity (Figure 7b). This is in good agreement with the numerical simulations and a mean value of turbulent dissipation rate at the surface of the membrane between the rings being much larger for the patterned membranes.

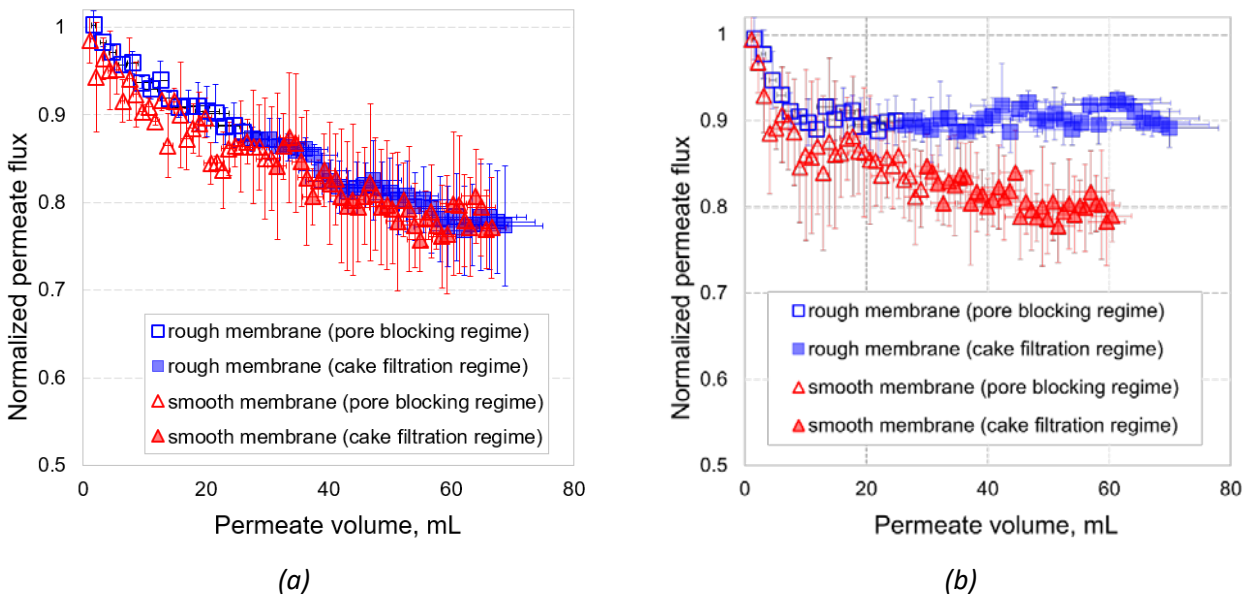


Figure 7. Normalized permeate flux recorded in crossflow filtration tests with smooth and rough membranes. (a) a crossflow velocity of  $0.45 \text{ m}\cdot\text{s}^{-1}$ ; (b) and a crossflow velocity of  $0.68 \text{ m}\cdot\text{s}^{-1}$ . Empty symbols correspond to the filtration stage where fouling is due to pore blocking while filled symbols correspond to the cake filtration regime.

#### 4.4. Considerations of scale

The fouling tests revealed a significant difference in roughness-induced mitigation of fouling between the two studied crossflow velocities. For a crossflow velocity of  $0.45 \text{ m}\cdot\text{s}^{-1}$ , the smooth and rough membranes seem to be affected by fouling phenomena in a similar way. For both membrane types, the permeate flux decreased by  $\sim 22 \%$  after 70 mL of permeate was collected. By contrast, significant differences were observed in tests with the crossflow velocity of  $0.68 \text{ m}\cdot\text{s}^{-1}$ ; in this case, whereas the smooth membranes exhibit the same 22 % flux decrease, the flux decline was only 10 % in experiments with the patterned filter. This result was very encouraging and provided the proof of concept of the patterned membranes.

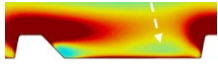
Near the membrane surface, between the rings, the dissipation rate of the turbulent kinetic energy ( $\varepsilon$ ) is multiplied by a factor 3.5 when the velocity is increase from  $0.45$  and  $0.68 \text{ m}\cdot\text{s}^{-1}$ . Turbulent energy dissipation rate  $\varepsilon$  is close to  $3 \text{ m}^2\cdot\text{s}^{-3}$  for  $v_{in} = 0.45 \text{ m}\cdot\text{s}^{-1}$  and  $10 \text{ m}^2\cdot\text{s}^{-3}$  for  $v_{in} = 0.68 \text{ m}\cdot\text{s}^{-1}$ , respectively (Table

2). Near the upper part of the rings, where the turbulence is the highest,  $\varepsilon$  is multiplied by a factor 5 when increasing the velocity (60 vs 300  $\text{m}^2\cdot\text{s}^{-3}$ ). The values of the Kolmogorov microscale,  $\kappa$ , are calculated using eq. (3) [26-28] and reported in Table 2.

$$\kappa = \left[ \frac{\eta^3}{\varepsilon} \right]^{1/4} \quad (3)$$

Whatever the location (between the rings corresponding to the lowest values of  $\varepsilon$ , or near the upper part of the rings corresponding to the highest values of  $\varepsilon$ ),  $\kappa$  increases 150 % with a decrease in the mean velocity from 0.68 to 0.45  $\text{m}\cdot\text{s}^{-1}$ .

Table 2. Kolmogorov microscale  $\kappa$  in low  $\varepsilon$  and high  $\varepsilon$  zones for two values of the average crossflow velocities

Location along the membrane surface	Mean crossflow velocity, $v_{in}$ ( $\text{m}\cdot\text{s}^{-1}$ )	Turbulent energy dissipation rate, $\varepsilon$ ( $\text{m}^2\cdot\text{s}^{-3}$ )	Kolmogorov microscale, $\kappa$ ( $\mu\text{m}$ )
Between the rings 	0.45	3.2	23.6
	0.68	10.5	17.6
Above the ring 	0.45	60	11.4
	0.68	300	7.6

Kolmogorov microscale corresponds to the lowest scale of turbulence, where viscosity dominates and the turbulent kinetic energy is dissipated. So,  $\kappa$  is often a relevant hydrodynamic parameter, which could be linked to fouling mechanisms. Notably, the values of  $\kappa \sim$  two orders of magnitude smaller than characteristic dimensions of roughness features - the size of the rings ( $\sim 1.5$  mm) or the inter-ring distance ( $\sim 3$  mm). Thus, based on purely scale-based considerations, the improvement in permeate flux (Figure 7b) is tentatively attributed to the disruption of the filter cake growth at the scale on several microns (i.e.  $\sim \kappa$   $\mu\text{m}$ ). Even if the fouling mechanisms are complex and their mitigation could be linked to several phenomena, the significant increase of the dissipation rate of the turbulent kinetic energy and the associated decrease of the Kolmogorov microscale are in good agreement with the fouling results reported in Figure 7.

#### 4.5. Potential of stereolithography for ceramic membrane design

Through creating desired surface morphology at the nanoscale, additive manufacturing methods help control flow to mitigate deposition of colloids and larger particle and, thereby, mitigate membrane fouling. However, the methods impose limitations on the material properties of the membrane that supports such surface features. First, small alumina particle size helps improving both the spatial resolution of the stereolithography method and the mechanical properties of membranes post-sintering; however, the smaller size of the primary particles leads to a low final pore size. The pore diameter of  $\sim 0.2$   $\mu\text{m}$  reported in this work is more than an order of magnitude smaller than the pore size achievable by extrusion of

pastes formulated from coarser and monodispersed powders. Addition of pore-forming agents in the stereolithography formulation is thus recommended to increase the pore size and achieve a better balance between resolution and permeability. Second, symmetrical patterned microfiltration membranes could be used as a porous support for the production of patterned ultrafiltration or nanofiltration membranes by deposition of successive thin layers by slip casting.

## **5. Conclusions**

CFD simulations were successfully used for guiding the design of 3D-printed tubular ceramic membranes and optimizing the surface morphology at the mesoscale in order to improve the hydrodynamic control of membrane fouling. CFD predictions were corroborated by the experimental data on membrane fouling. The mesoscale design of microfiltration membranes by additive manufacturing can be combined with preparing the lower porosity separation layer by conventional methods of separation layer. Such optimal combination of membrane fabrication methods may be practically implemented through a multistep/multi-method morphological design as an alternative to changing the casting mixture composition for pore size control.

### **Author statement**

Cyril Chevarin: Methodology, Investigation, Analysis, Writing – Reviewing and Editing

Xunhao Wang: Methodology, Investigation, Analysis, Writing – Reviewing and Editing

Denis Bouyer: Conceptualisation, Methodology, Investigation, Analysis, Writing – Reviewing and Editing

Volodymyr V. Tarabara: Conceptualisation, Methodology, Investigation, Analysis, Writing – Reviewing and Editing

Thierry Chartier: Conceptualisation, Methodology, Reviewing and Editing

André Ayral: Conceptualisation, Methodology, Analysis, Writing – Original Draft, Writing – Reviewing and Editing

### **Declaration of competing interest**

The authors declare that they have no known competing financial interests or personal relationships that could have appeared to influence the work reported in this paper.

### **Acknowledgments**

We are grateful to Mr. Didier Cot and Dr. Martin Drobek (both at Institut Européen des Membranes) for performing SEM and Hg porosimetry analyses, respectively. We also thank 3DCERAM SINTO (Limoges, France) for the manufacturing the prototype membranes and providing them to our team. This material is

based upon work supported in part by the U.S. National Science Foundation under grant No. OISE-1952438, which supported the cooperation between Institut Européen des Membranes and Michigan State University.

## References

- [1] T. Chartier, A. Badev, Rapid Prototyping of Ceramics, in: S. Somiya, M. Kaneno (Eds.) Handbook of Advanced Ceramics, 2013, pp. 489-524.
- [2] T. Chartier, C. Dupas, M. Lasgorceix, J.D.N. Brie, C. Chaput, Additive manufacturing to produce complex 3D ceramic parts, *J. Ceram. Sci. Technol.*, 6 (2014) 95-104.
- [3] Z. Chen, Z. Li, J. Li, C. Liu, C. Lao, Y. Fu, C. Liu, Y. Li, P. Wang, Y. He, 3D printing of ceramics: A review, *J. Eur. Ceram. Soc.*, 39 (2019) 661-687.
- [4] T. Chen, D. Wang, X. Chen, M. Qiu, Y. Fan, Three-dimensional printing of high-flux ceramic membranes with an asymmetric structure via digital light processing, *Ceram. Int.*, 48 (2022) 304-312.
- [5] H. Dommati, S.S. Ray, J.-C. Wang, S.-S. Chen, A comprehensive review of recent developments in 3D printing technique for ceramic membrane fabrication for water purification, *RSC Adv.*, 9 (2019) 16869.
- [6] D. Wang, T. Chen, Y. Zeng, X. Chen, W. Xing, Y. Fan, X. Qiao, Optimization of UV-curable alumina suspension for digital light processing of ceramic membranes, *J. Membr. Sci.*, 643 (2022).
- [7] H.A. Balogun, R. Sulaiman, S.S. Marzouk, A. Giwa, S.W. Hasan, 3D printing and surface imprinting technologies for water treatment: A review, *J. Water Process. Eng.*, 31 (2019) 100786.
- [8] T. Femmer, A. Kuehne, J. Torres-Rendon, A. Walther, M. Wessling, A.J. Kuehne, Print your membrane: Rapid prototyping of complex 3D-PDMS membranes via a sacrificial resist, *J. Membr. Sci.*, 478 (2015) 12-18.
- [9] M.N. Issac, B. Kandasubramanian, Review of manufacturing three-dimensional-printed membranes for water treatment, *Environ. Sci. Pollut. Res.*, 27 (2020) 36091-36108.
- [10] J.-Y. Lee, W.S. Tan, J. An, C.K. Chua, C.Y. Tang, A.G. Fane, T.H. Chong, The potential to enhance membrane module design with 3D printing technology, *J. Membr. Sci.*, 499 (2016) 480-490.
- [11] Z.-X. Low, Y.T. Chua, B.M. Ray, D. Mattia, I.S. Metcalfe, D.A. Patterson, Perspective on 3D printing of separation membranes and comparison to related unconventional fabrication techniques, *J. Membr. Sci.*, 523 (2017) 596-613.
- [12] W. Choi, C. Lee, D. Lee, Y.J. Won, G.W. Lee, M.G. Shin, B. Chun, T.-S. Kim, H.D. Park, H.W. Jung, J.S. Lee, J.-H. Lee, Sharkskin-mimetic desalination membranes with ultralow biofouling, *J. Mater. Chem. A*, 6 (2018) 23034-23045.
- [13] Y.-J. Won, S.-Y. Jung, J.-H. Jang, J.-W. Lee, H.-R. Chae, D.-C. Choi, K.H. Ahn, C.-H. Lee, P.-K. Park, Correlation of membrane fouling with topography of patterned membranes for water treatment, *J. Membr. Sci.*, 498 (2016) 14-19.
- [14] Z. Zhao, A. Ilyas, K. Muylaert, I.F. Vankelecom, Optimization of patterned polysulfone membranes for microalgae harvesting, *Bioresour. Technol.*, 309 (2020).

- [15] Z. Lyu, T.C.A. Ng, T. Tran-Duc, G.J.H. Lim, Q. Gu, L. Zhang, Z. Zhang, J. Ding, N. Phan-Thien, J. Wang, H.Y. Ng, 3D-printed surface-patterned ceramic membrane with enhanced performance in crossflow filtration, *J. Membr. Sci.*, 606 (2020) 118138.
- [16] T.C.A. Ng, Z. Lyu, C. Wang, S. Guo, W. Poh, Q. Gu, L. Zhang, J. Wang, H.Y. Ng, Effect of surface-patterned topographies of ceramic membranes on the filtration of activated sludge and their interaction with different particle sizes, *J. Membr. Sci.*, 645 (2022).
- [17] Z. Yang, J. Cheng, C. Yang, B. Liang, CFD-based optimization and design of multi-channel inorganic membrane tubes, *Chin. J. Chem. Eng.*, 24 (2016) 1375-1385.
- [18] L. Broussous, P. Schmitz, E. Prouzet, L. Becque, A. Larbot, New ceramic membranes designed for crossflow filtration enhancement, *Separ. Purif. Technol.*, 25 (2001) 333-339.
- [19] P.A. Lescoch, J., Game changer in inorganic membranes, in: ICIM 2018, Dresden, 2018.
- [20] B.E. Launder, D.B. Spalding, The numerical computation of turbulent flows, *Comput. Method. Appl. Mechanics Eng.*, 3 (1974) 269-289.
- [21] W.P. Jones, B.E. Launder, The prediction of laminarization with a two-equation model of turbulence, *Int. J. Heat Mass Transfer*, 15 (1972) 301-314.
- [22] A. Einstein, A New Determination of Molecular Dimensions, *Ann. Physik*, 34 (1911) 591.
- [23] M. Herzberg, M. Elimelech, Biofouling of reverse osmosis membranes: Role of biofilm-enhanced osmotic pressure, *J. Membr. Sci.*, 295 (2007) 11-20.
- [24] F. Wang, V.V. Tarabara, Pore blocking mechanisms during early stages of membrane fouling by colloids, *J. Colloid Interface Sci.*, 328 (2008) 464-469.
- [25] C.J. Brinker, Scherer, G. W., *Sol-Gel Science: The Physics and Chemistry of Sol-Gel Processing*, 1990.
- [26] A.N. Kolmogorov, The local structure of turbulence in incompressible viscous fluid for very large Reynolds numbers, *Dokl. Akad. Nauk. SSSR*, 30 (1941) 299-303.
- [27] A.N. Kolmogorov, The local structure of turbulence in incompressible viscous liquid, *Dokl. Akad. Nauk. SSSR*, 31 (1941) 538-541.
- [28] A.N. Kolmogorov, Dissipation of energy in locally isotropic turbulence, *Dokl. Akad. Nauk. SSSR*, 32 (1941) 19-21.